Chapter

Skyrmions in Thin Films, Interfaces and Antiferromagnetism

Rajesh Kumar Rajagopal

Abstract

Magnetic skyrmions are small whirling topological defects in a texture magnetization state. Their stabilization and dynamics depend strongly on their topological properties. Skyrmions are induced by non-centrosymmetric crystal structure of magnetic compounds and thin films. Skyrmions are extremely small, with diameters in the nanometer range, and behave as particles that can be created, moved and annihilated. This makes them suitable for information storage and logic technologies. Skyrmions had been observed only at low temperature, and mostly under large applied magnetic fields. An intense research in this field has led to the identification of skyrmions in thin-film and multilayer structures in these heterostrutres skyrmions are able to survive at room temperature and can be manipulated by electrical currents. Utilizing interlayer magnetic exchange bias with synthetic antiferromagnet with can be used to isolated antiferromagnetic skyrmions at room temperature. The development of skyrmion-based topological spintronics holds promise for applications in the writing, processing and reading functionalities at room temperature and can be extended further to all-electrical manipulation spintronics.

Keywords: Skyrmions, thin films, interfaces, magnetism, multilayers

1. Introduction

Skyrmions in magnetic materials are topological spin textures that are stabilized in various types of magnetic interactions. Non-centrosymmetric bulk magnetic materials exhibit chiral, polar, or D_{2d} symmetry which provide a good area to study the topological spin structures and emergent electromagnetic responses arising from them [1, 2]. In these materials without the presence of inversion symmetry, Dzyaloshinskii–Moriya interaction (DMI) can gradually twists the ferromagnetic spin arrangement, giving rise to helimagnetic structure in zero field as well as skyrmions in presence of a magnetic field. The stabilization of Skyrmions is not only due to deformation of helical spin structure but the topologically protected state from external perturbations and thus appropriate for carrying information in robust manner. Skyrmions can be different in to three types of as schematically shown in **Figure 1** have been observed experimentally, which were theoretically predicted Such as Bloch, Néel and Anti skyrmions [3].

Bloch-type skyrmions Bloch-type skyrmion is the first category in chiral magnetic materials, where the spins are lying within the tangential plane of the system,

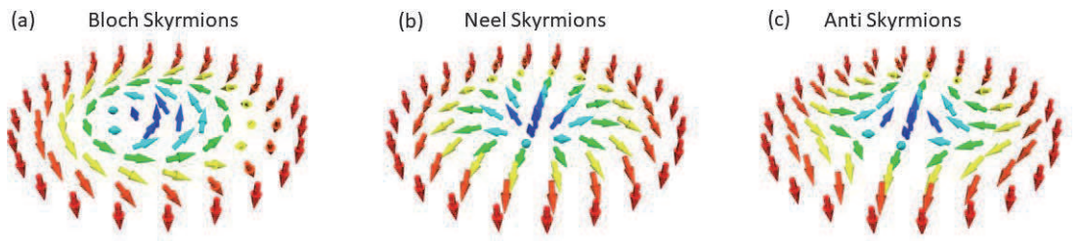

Figure 1.
(a) Bloch-type skyrmion is observed by a transverse helix with an anticlockwise spin rotation, (b) Néel-type magnetic skyrmion is observed by the anticlockwise-rotated magnetization in a spin cycloid and (c) antiskyrmion has a structure of boundary walls that have alternating Bloch and Néel types.

as shown in **Figure 1(a)**. It was first experimentally observed in the A-phase of MnSi with B20-type chiral magnetic structure. The skyrmion structure is described as a superposition of three screw-type helices, by small angle neutron scattering (SANS) [4] and later by Lorentz transmission electron microscopy (LTEM) technique [5]. Later on other bulk systems, in 2012, skyrmions were observed in multiferroic Cu_2OSeO_3 [6]. In 2015, β-Mn type Co-Zn-Mn alloy showed metastable skyrmion at zero magnetic field and room temperature [7], as displayed in **Figure 2**. The formation of the skyrmions was confirmed in the real space by Lorentz transmission electron microscopy (LTEM) along the (110) direction of the sample and it thickness was 150 nm. The skyrmions state was seen at 370 K at the 0.07 T magnetic field and it was persistant till 290 K during the field cooled process. The Skyrmions state was not influenced by the field cooling protocol. The characteristic swirling of the magnetic moments in a skyrmion is observed by the angular color coding in **Figure 2**. In the zero field protocol the magnetic skyrmions are seen also at 350 K and the helical state was seen at 370 K.

Néel-Type skyrmions Néel-type of skyrmion is the second class of skyrmions. It is observed in polar magnets with the spins are lying within a radial plane, as shown in **Figure 1(b)**, and their lattice is described as a superposition of three cycloidal helices. The bulk material of GaV_4S_8 identified to show Néel-type skyrmion which is a polar compound with a Lacunar spinel structure (**Figure 3**) [8].

Antiskyrmions Antiskyrmion is the third type in the skyrmion family as shown in **Figure 1(c)**. It's structure can be understood in terms seeing along the cross-sections of an antiskyrmion with either screw-type helix or cycloidal one, depending on the azimuthal direction of observance. It was discovered in Heusler compounds with D_{2d} crystal symmetry in 2017 and experimental observed using LTEM **Figure 4** [9]. Application of magnetic fields stabilizes the antiskyrmion in the lattice in the wide range temperature including room temperature. The antiskyrmions in thesystem in detail, an under-focused LTEM image of a single antiskyrmion taken at a field of 0.29 T applied parallel to the [001] direction is displayed in **Figure 4(a)**. Most interestingly, it exhibits two bright spots and two dark spots along the [010] and [100] directions, respectively. The modulation of the contrast can be discerned from the appearance of two peaks with a trough in the middle of the line profile taken along [010] (lower inset) and two troughs with a peak in the middle of the line profile taken along [100] (upper inset). A slight distortion of the lattice along [010] might be related to the presence of a small amount of in-plane field due to a slight misorientation (by approximately $\pm 3°$) of the sample away from the exact [001] direction. At low in-plane fields, the distortion is mostly in the [010] direction as the helix propagates along [100]. Owing to the tetragonal D2d symmetry, we expect that the antiskyrmion lattices undergo characteristic distortions in oblique fields, because their axis remains locked to the tetragonal axis, and that the antiskyrmions are consequently distorted, with the perfectly radial core shifting from the centres of the cells of the hexagonal densely

DOI: http://dx.doi.org/10.5772/intechopen.97636

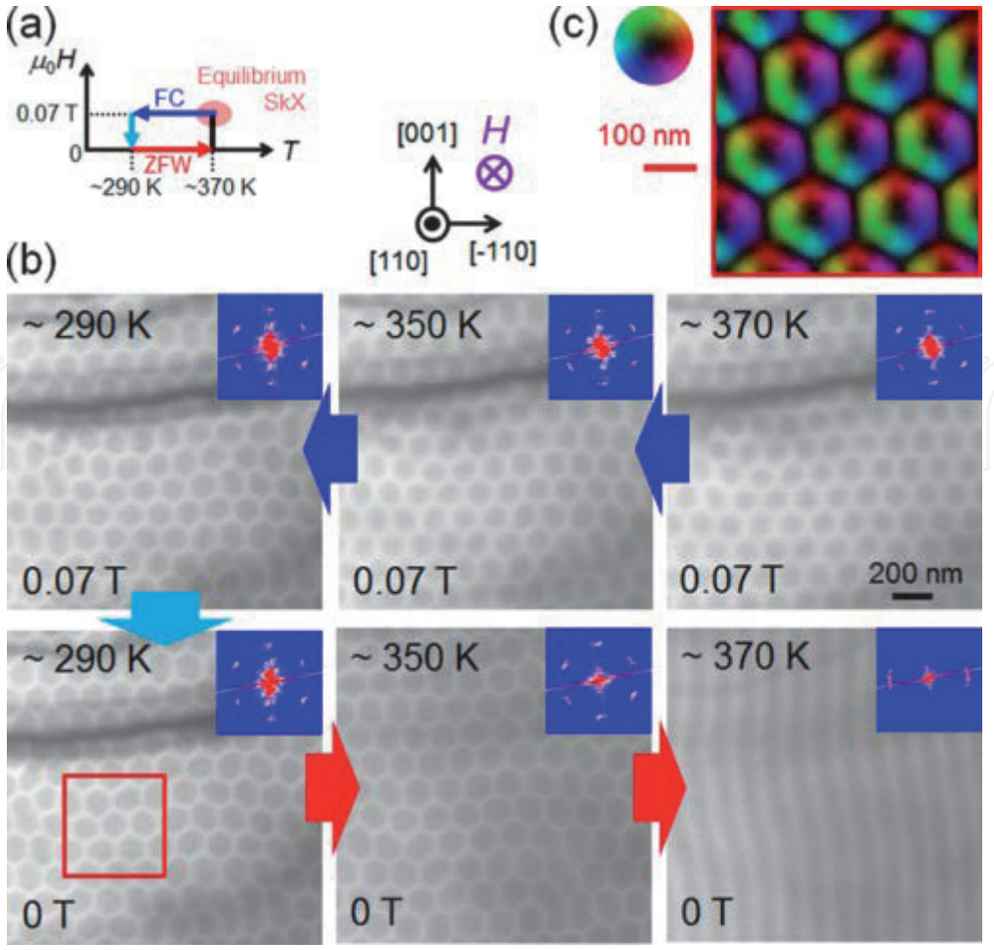

Figure 2.
Schematic illustration of the measurement process. The colors of the arrows correspond to the colors of arrows in (b). (b) Overfocused LTEM images on the (110) plane in the FC process and in the subsequent ZFW process. The defocus values of LTEM images were set to be +28 8μm at 370 K,192 μm at 350 K, and + 96 μm at 290 K, respectively. These LTEM images were taken for nearly the same sample position. The insets of the respective panels show the fast Fourier-transformed patterns of the LTEM images taken over a wider sample area. (c) Distribution of in-plane magnetic moments for the area indicated by the red square in (b) at 290 K and zero magnetic field after the FC, as deduced from a transport-of-intensity equation analysis of overfocused and underfocused LTEM images. The color wheel represents the direction and magnitude of the in-plane magnetization [7].

packed lattice. in **Figure 4(d)**, illustrating the skewed appearance of the antiskyrmions. This effect occurs because the in-plane component of the magnetic field favors and broadens one edge of the circulating magnetization along the field, at the cost of the opposite edge. As can be seen in **Figure 4(e)**, when a magnetic field was applied at an angle of about 20 degrees to [001] by rotating the sample along [110], the antiskyrmions become distorted. We find that the antiskyrmions are stable up to this maximum possible tilt angle. The appearance of double-skyrmion-like features results from the projection of the antiskyrmion tubes that are oriented obliquely to the illuminating electron beam and to the applied field. As the rotation angle decreases (**Figure 4e–g**), the original quadrupole-like internal magnetization distribution of the antiskyrmions is revealed. Strong bright spots can be seen at the upper half of the antiskyrmions for a rotation angle of θ = 8 (**Figure 3g**), whereas they appear at the lower half for θ = 5° (**Figure 4** (h)). In both cases, the antiskyrmion lattice exhibits a large distortion along [010]. Nearly symmetric bright and dark spots in an almost hexagonal lattice can be seen in **Figure 4(i)**, for an applied field of 0.29 T along [001] (within the ±3° limit). A small increase in the field to 0.33 T perturbs the regular arrangement of the antiskyrmions in the lattice **Figure 4** (j). This field corresponds to the stability limit of the equilibrium

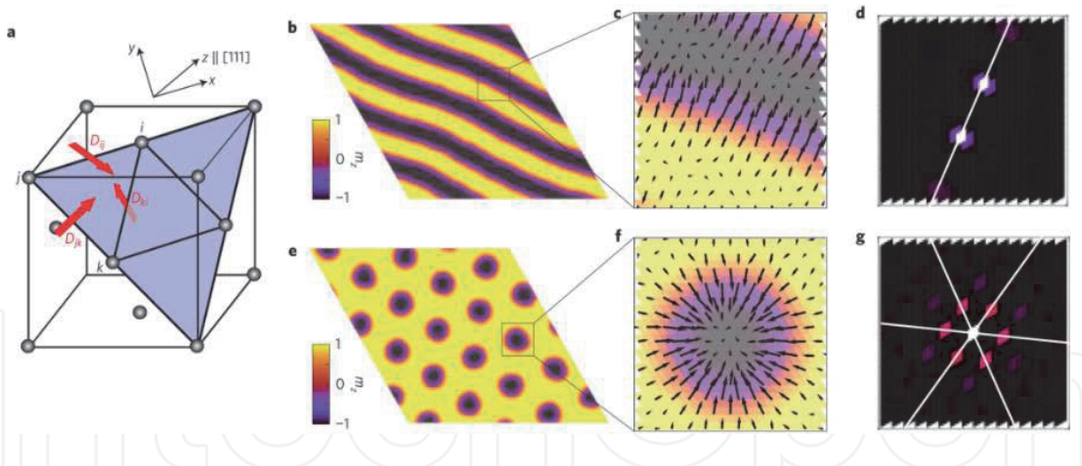

Figure 3.
a, FCC lattice of V4 units, each carrying a spin 1/2, and the orientation of the Dzyaloshinskii–Moriya vectors for bonds on the triangular lattice within the (111) plane (chosen as the xy plane in the calculation). b, Cycloidal spin state obtained for the spin model in equation (1) on the triangular lattice in zero magnetic field. The color coding indicates the out-of-plane components of the spins. c, magnified view of the magnetization configuration for the cycloidal state. The arrows correspond to the in-plane components of the spins at every second site of the triangular lattice. (The remainder of the sites are not shown to reduce the density of the arrows and preserve the clarity of the figure.) d, Bragg peaks (q-vectors) of the cycloidal state in b in reciprocal space. e, SkL state obtained for the spin model in equation (1) (To determine the spin patterns classical Heisenberg model on the triangular lattice was carried out by Monte Carlo technique) on the triangular lattice for B/J⊥ = 0.08 along the z axis. The color coding is the same as in b. f, Magnified view of the magnetization configuration for the SkL state clearly shows the Néel-type domain wall alignment. Note that the magnetization points opposite to the magnetic field in the core region of the skyrmions. (Similarly to c, only every second spin is shown.) g, Bragg peaks of the SkL state in e. The q-vectors of first-order Bragg peaks are located along the ~10~ directions (white lines) in the hard plane, for both the cycloidal and SkL states [8].

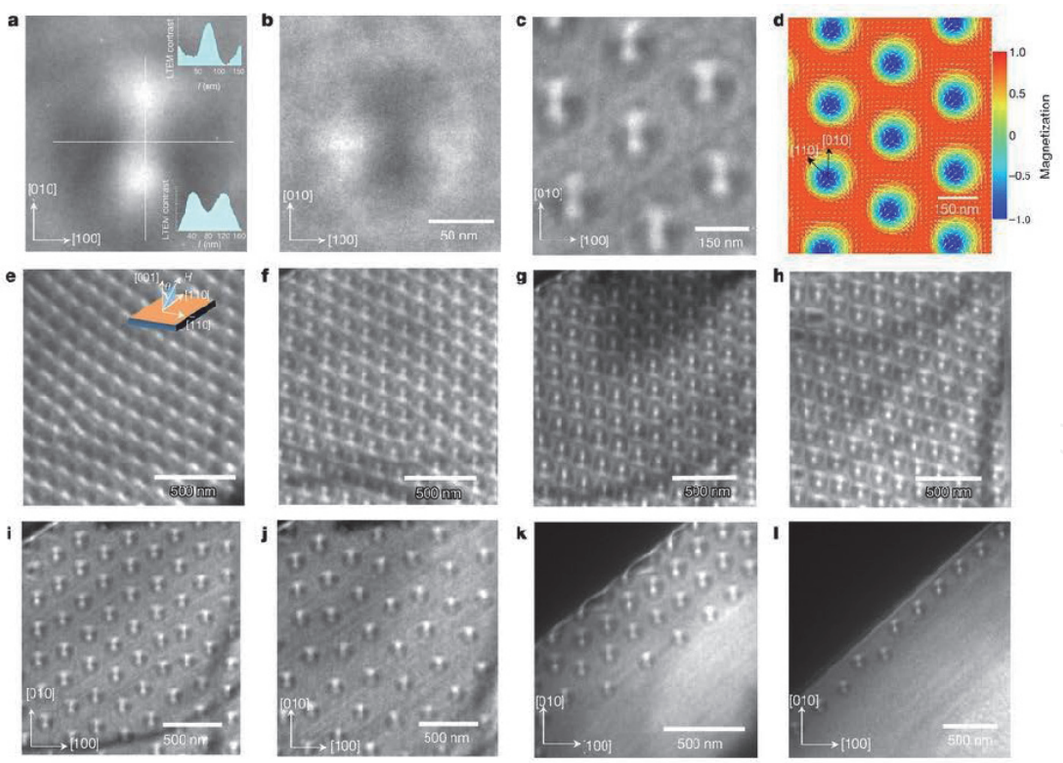

Figure 4.
Under-focused LTEM image of a single antiskyrmion at 300 K and with a field (0.29 T) applied along [001]. The lower and upper insets show the intensity profiles of the in-plane magnetization along [010] and [100], respectively. The corresponding scanned regions are marked by lines. I, distance. b, Over-focused LTEM image of the single antiskyrmion shown in a. c, Under-focused LTEM image showing a hexagonal lattice of antiskyrmions. d, Theoretical simulation of an antiskyrmion lattice in an oblique field. The color represents the magnetization component normal to the sample plane. E–h, under-focused LTEM images of antiskyrmions taken at 300 K and in H = 0.24 T with rotation angles (θ; as shown schematically in the inset of e) of θ = 20° (e), θ= 13° (f), θ = 8° (g) and θ =5° (h). i–l, Under-focused LTEM images of antiskyrmions taken at fields applied along [001] of 0.29 T (i), 0.33 T (j), 0.24 T (k) and 0.49 T (l) [9].

lattice phase. Owing to their topological stability, a large number of antiskyrmions remain as metastable excitations in the homogeneous field-polarized collinear state. For even higher fields, antiskyrmions disappear from the relatively thinner region of the sample and are stabilized only in the thicker region (**Figure 4(k)**). Finally, the antiskyrmion lattice evolves into an array of single antiskyrmions, which disappear for fields above 0.49 T at room temperature (**Figure 4(l)**).

It can be observed that some materials exhibit (anti)skyrmions above room temperature, but continued efforts to has been made in this area to expand the horizon of such materials and necessary understanding of the fundamental physics of the skyrmions is required for their device applications. Further three-dimensional nature of skyrmions in non-centrosymmetric bulk materials can provide unique functionalities where the directionally non-reciprocal transmission of spin excitations can be manipulated. The spin excitations are difficult to observe for interfacial-DMI-based skyrmions in magnetic multilayer systems. **In the following sections, we describe current and future challenges, followed by advances in science and technology to meet them, which are commonly important for all the three types of bulk skyrmions.**

2. Skyrmions in mono layer thin films and multilayer interfaces

From the previous section it can be observed that the magnetic skyrmions were initially identified in single crystals of magnetic materials with a non-centrosymmetric lattice [4, 5], and explained by the existence of DMIs induced by spin–orbit coupling in the absence of inversion symmetry in the crystal lattice.

2.1 Monolayer epitaxial thin films

Skyrmions were observed in epitaxial ultrathin magnetic films grown on heavy metals, which are subject to gaint DMIs induced at the interface that breaks inversion symmetry and the strong spin–orbit coupling with neighboring heavy metal. The first investigated systems in this class were Fe monolayers and PdFe bilayers on Ir(111), huge DMI was seen at the interface of Fe/Ir(111) [10]. Skyrmions observed in these systems are extremely small and was extending for only a few lattice parameters (5(c)). However, the skyrmions are stabilization in large magnetic fields of 1 T and low temperatures and at low temperature of 30 K. Moreover, the skyrmion lattice ground state of an Fe monolayer on Ir(111) does not allow the specific properties of individual skyrmions to be exploited. In PdFe bilayers epitaxially grown on Ir(111), spin spirals are observed at low field with an applied field of about 1 T induces a ferromagnetic state embedding individual metastable skyrmions transition to a [11].

The a two-dimensional square lattice of skyrmions was observed on a single atomic length scale. The magnetic ground state of a hexagonal Fe film of one-atomic-layer thickness on the Ir(111) surface. The real space image of skrmion was imaged using the Using spin-polarized scanning tunneling microscopy by which we can directly image the non-collinear spin texture in and demonstrate that it is incommensurate to the underlying atomic lattice [10]. To investigate the magnetic ground the measurements were carried out with and without an external magnetic field using a tip sensitive to the in-plane magnetization component of the sample. The SP-STM image measured with an in-plane magnetized tip is shown **Figure 5a**, shows all three possible rotational magnetic domains due to the combination of square magnetic structure and a hexagonal atomic lattice. Using the of the tip with one particular magnetization they were able to catch different components of the

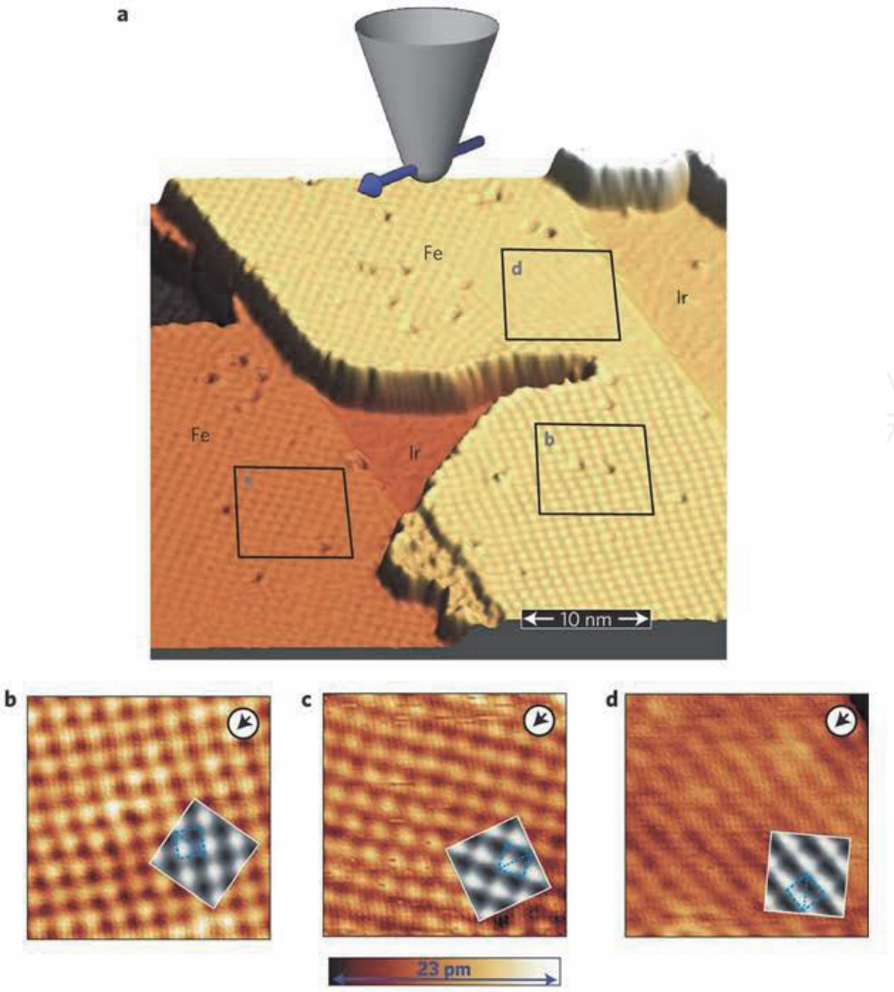

Figure 5.
(a) Three-dimensional representation of a sample area with all three possible rotational magnetic domains measured with a tip sensitive to the in-plane component of magnetization as shown (Fe-coated W tip, U = +5 mV, I = 0.2 nA, sketched tip magnetization axis inferred from comparison to simulated SP-STM images). B–d, closer views of the three rotational domains indicated by squares in a; the tip magnetization is indicated by the arrows. Insets: The simulations of SP-STM measurement of the nanoskyrmion with this tip magnetization; image size and unit-cell position identical owing to the relation between the three rotational domains the magnetic unit cell is rotated by 120° from domain to domain. Note the color scale applies to b–d only [10].

in-plane sample magnetization of the rotational domains with respect to a unique axis in the magnetic unit cell. A closer view of each magnetic domain is shown in **Figure 5**(**b–d**). We can analyze the images by considering that all of them have been measured with an identical magnetic tip and the tips magnetization direction indicated by arrows) while the magnetic unit cell rotates by 120° from domain to domain. The excellent agreement between SP-STM experiment and simulated images in the insets clearly shows that our magnetic structure is in accordance with the nanoskyrmion lattice. Based on SP-STM measurements for the in-plane and out-of-plane magnetization components we can even construct the vector magnetization density of our sample, revealing the characteristic spin structure of the skyrmion lattice. **Figure 5d**, is at the resolution limit of STM which is about one-third of that for the square patterns **Figure 5b,c** and seems to require a very high spin polarization of the tip. However, the observation of this pattern in a simultaneous measurement on three different domains–which has not been possible in a previous measurement–is crucial to unambiguously identify magnetic in-plane sensitivity. By applying an in-plane magnetic field, we can align the tip magnetization direction with respect to the crystallographic directions and experimentally rule out

a vortex lattice, which could also explain the measurement of **Figure 5**. The reading and writing of the magnetic domains was demonstrated by using the topological property of the skyrmions [11]. By injecting electrons locally they have we generated the desired skyrmion configuration for the four pinning sites within the area. In the series of difference SP-STM images in **Figure 6(b)** to **(e)**, the skyrmions are annihilated one after the another until no skyrmion is present as shown in **Figure 6(f)**. The skyrmions are then created in a different sequence until the starting part of the configuration is reached again as shown in the **Figure 6(g)** to **(j)**. By sweeping the voltage locally the writing and deleting was done. These measurements have demonstrated that the skyrmions can be manipulated individually and independently in a close proximity to one another.

The chiral magnets with archetypal B20 family like MnSi, $Fe_xCo_{1-x}Si$, FeGe, $Fe_{1-x}Co_xGe$, $Fe_{1-x}Mn_xGe$ and MnGe [12, 13]. These B20 silicides and germanides lattice matches well with Si(111) and can be grown epitaxially on the technologically relevant substrates like MgO and SiC(0001). High quality films on large substrates area create the possibility to explore the influence of anisotropy and finite size effects on chiral magnets. Anisotropy provides an important mechanism for increasing the skyrmion stability, which is enhanced along the easy direction, or in an easy-plane, but is reduced along a hard-axis or in a hard-plane relative to the competing cone phase The micromagnetic calculations for MnSi [12], shown in **Figure 7(a)**, indicate that a skyrmion in grating are more energetically favorable than the helicoids. The spin asymmetry scattering expected from the one dimenaional helicoidal modulation does not agree with the measured asymmetry. In the sample interfacial twists at the chiral grain boundaries repel skyrmions and restrict their elliptic distortion below the strip-out field. The energy barriers associated with the film interfaces and grain boundaries lead to metastable structures consisting of helicoid as shown in **Figure 7(b)** [13]. The repulsive force imposed by the surface twist of helimagnet creates lateral confining potential for moving skrmions along the centre of as shown in **Figure 7(c)** [14] Finite size effects arise from the presence of DMI in the zero-torque boundary conditions, which creates surface states that decay into the bulk of the film on a length scale set by the helical

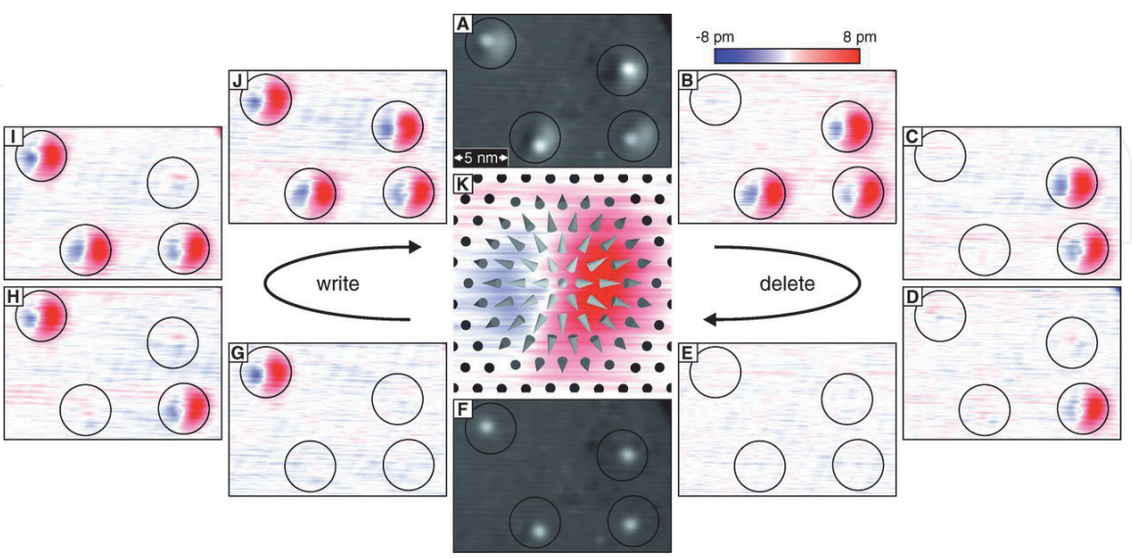

Figure 6.
(a) Constant-current image of a sample region with four defects each hosting a skyrmion marked by a circle containing 270 surface atoms (V = +250 mV, I = 1 nA, B = +3.25 T, T = 4.2 K, magnetically in-plane tip. (b) to (e) Sequence of difference SP-STM images with respect to (f) showing the selective erasing of all four skyrmions using local voltage sweeps. (f) The sample area without skyrmions in a constant-current mode and (g) to (j) their successive rewriting with the difference images. (k) Is the schematic spin configuration with distances twice the atomic lattice, superimposed on the experimental data [10].

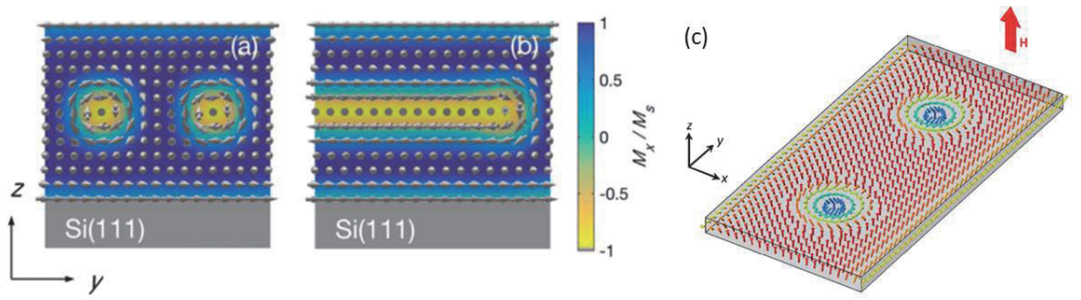

Figure 7.
The calculation of the magnetization M on the y-z plane of (a) 26.4-nm-thick MnSi film where the color plot corresponds to mx. (a) Skyrmiongrating for a field of $\mu_0 H = 0.5$ T. (b) Half of a metastablehelicoidal structure at a field of $\mu_0 H = 0.3$ T, formed from a skyrmion when the applied field is dropped below the skyrmion elliptic instability. (c) Repulsive chiral surface twists that arise at the edges of a narrow strip of a saturated helimagnet force isolated skyrmions to move along the central line of the strip [12].

wavelength, LD and the applied magnetic field. One-dimensional surface twists first were first observed in polarized neutron reflectometry measurements in the field induced ferromagnetic state of MnSi/Si(111) [12]. These twists produce a confining potential for skyrmions that is crucial for devices, since film edges remove the skyrmions' topological protection [14]. Micromagnetic calculations show that the surface states produce a cross-over in the magnetic behavior for film thicknesses below approximately 8LD, where skyrmions are stabilized over a large portion.

2.2 Multilayer thin films

In multilayers for the skyrmions are formed by stacking layers of magnetic and non-magnetic heavy thin metallic films [15, 16]. These multilayer exhibit promising results on the observation of individual skyrmions. Where as in the monolayer a collection of skyrmions are observed. The multilayer approach offers advantages and opportunities for tailoring the skyrmion characteristics. By changing tuning the interactions with different material combination between magnetic metals, heavy metals, ferroelectrics and by varying the number of repetitions in the multilayers.

The multilayered structure combines the interface-driven, out-of-plane magnetic anisotropy and additive DMI at successive interfaces [16, 17]. The room temperature skyrmions have been recently obtained in for example, those formed by 10 repetitions of 0.6 nm of Co sandwiched between 1 nm of Ir and 1 nm of Pt — the additive DMI at the Co/Ir and Co/Pt interfaces [15, 16] induces skyrmions in the Co layers. The skyrmions in successive Co layers are coupled through the ultrathin non-magnetic layers, the large magnetic volume of the resulting along the columns of the thin film of couples. The Monte Carlo simulations for fcc stacking of the Pd overlayer is displayed the low-temperature phase diagram as shown in **Figure 8a**. At zero magnetic field an spin spiral state with a period of about 3 nm is shown in **Figure 8b**. In the lattice the distance between adjacent skyrmions amounts to about 3.3 nm and the system undergoes a second phase transition into the saturated ferromagnetic state for magnetic fields above 17 T. The two phase boundaries metastable state are mixed and appear on cooling down the sample in a finite magnetic field, for example, composed of spin spirals and single skyrmions in **Figure 8c**. For larger fields the isolated skyrmions in a homogeneous ferromagnetic background.

The magnetic properties in spin glasses revealed that chiral magnetic interactions between neighboring spins can also play a key role in metallic systems. The RKKY model was extended to 3-sites to the bilayer systems has been predicted by [18] that a large Dzyaloshinskii–Moriya interaction (DMI) with magnetic film and a

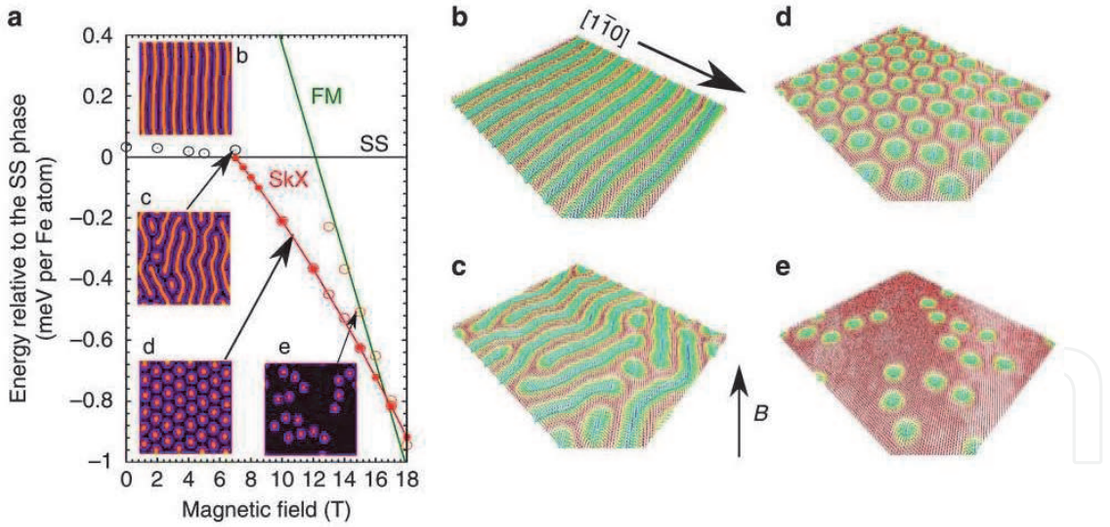

Figure 8.
(a) Phase diagram for fcc stacking of the Pd overlayer on the Fe ML on Ir(111) at low temperatures as a function of a magnetic field applied perpendicular to the film. The energy per Fe atom of the spin spiral (SS), the skyrmion lattice (SkX) and the saturated ferromagnetic (FM) state are given by black, red and green lines, respectively. Open circles indicate the energy of mixed states. Insets show the simulated spin-polarized scanning tunneling microscopic images for an out-of-plane magnetized tip of the spin structures that are displayed in b–e. (b–e) A red color denotes magnetic moments pointing up, that is, in the direction of the magnetic field, while blue spins point into the opposite direction [15].

heavy material with large spin–orbit coupling. The best solution up to now seems to increase the effective magnetic volume by using multilayer stacks composed of multiple repetitions of thin magnetic metal layers separated by heavy metal nonmagnetic layers grown by sputtering deposition. This approach enables the increase of the thermal stability of columnar skyrmions, that are coupled in the successive layers, leading to the recent observation of sub-100 nm skyrmions stable at RT in different multilayer systems [19, 20]. The quasi static XMCD-STXm images

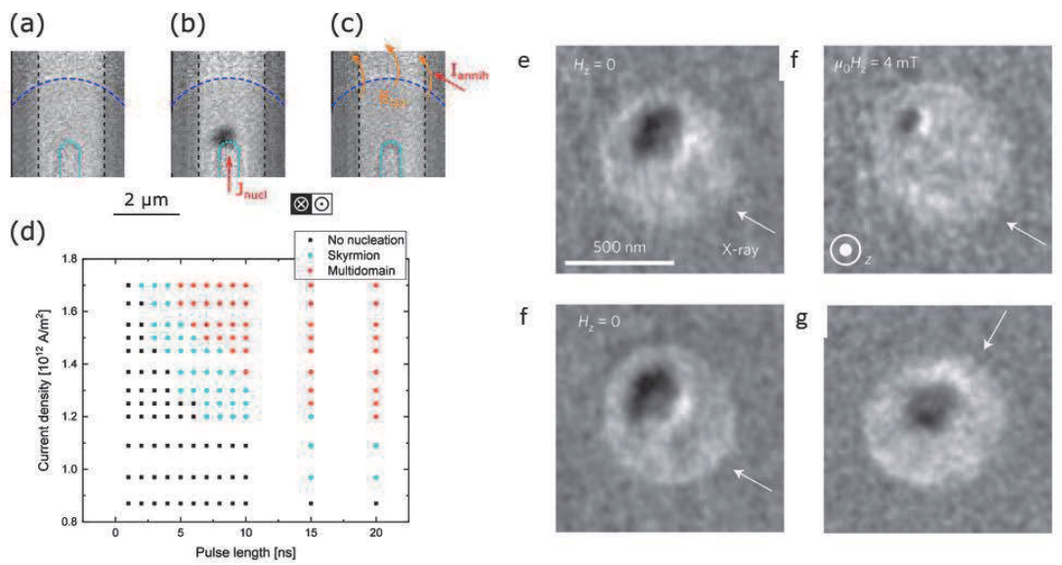

Figure 9.
(a–c) XMCD-STXM images of the current-induced nucleation and field-induced deletion of a magnetic skyrmion in the quasi-static mode, (b) nucleation of a magnetic skyrmion, (c) recovery of the initial magnetic configuration by injecting a current pulse across the microcoil, leading to the generation of an out-of-plane magnetic field pulse and (d) dependence of the current density required to nucleate an isolated magnetic skyrmion on the duration of the current pulse injected (e), XMCD-PEEM image of a magnetic skyrmion in a 630 nm diameter circular dot. (f), XMCD-PEEM image of the same skyrmion during the application of an external magnetic field perpendicular to the film plane μ0Hz = 4 mT. (g), image taken after b for H_z = 0. (h), XMCD-PEEM image of the skyrmion after rotation of the sample by 90° with respect to the X-ray beam direction. The white arrows indicate the direction of the X-ray beam.

were carried out as shown in **Figure 9(a-c)**, the nucleation and the detection of the protocol employed. The **Figure 9(b)** shows the nucleation of the magnetic skyrmions by the 5 ns current pulse and the recovery if the initial configuration by the microcoil as shown in **Figure 9(c)** and the skyrmion nucleation and their window can be observed from these measurement is shown in **Figure 9(d)**. **Figure 9(e)** shows the XMCD-PEEM image of a magnetic skyrmion with an 630 nm diameter. The larger skyrmion diameter of 190 nm is due to the larger Co thickness. When applying a field μ_0 Hz = 4 mT as shown in **Figure 9(f)** in the direction opposite to the skyrmion magnetization the size of the skyrmion decreases to 70 nm. When the external magnetic field is releasing the initial skyrmion structure is recovered as shown in **Figure 9(g)**. This demonstrates that the skyrmion structure is stable and reversible with respect to perturbations and that the skyrmion diameter can be tuned using frequency. The chiral structure of the skyrmion, we also imaged the skyrmion for an X-ray beam direction rotated by 90° in-plane with respect to the sample as shown in **Figure 9(h)**.

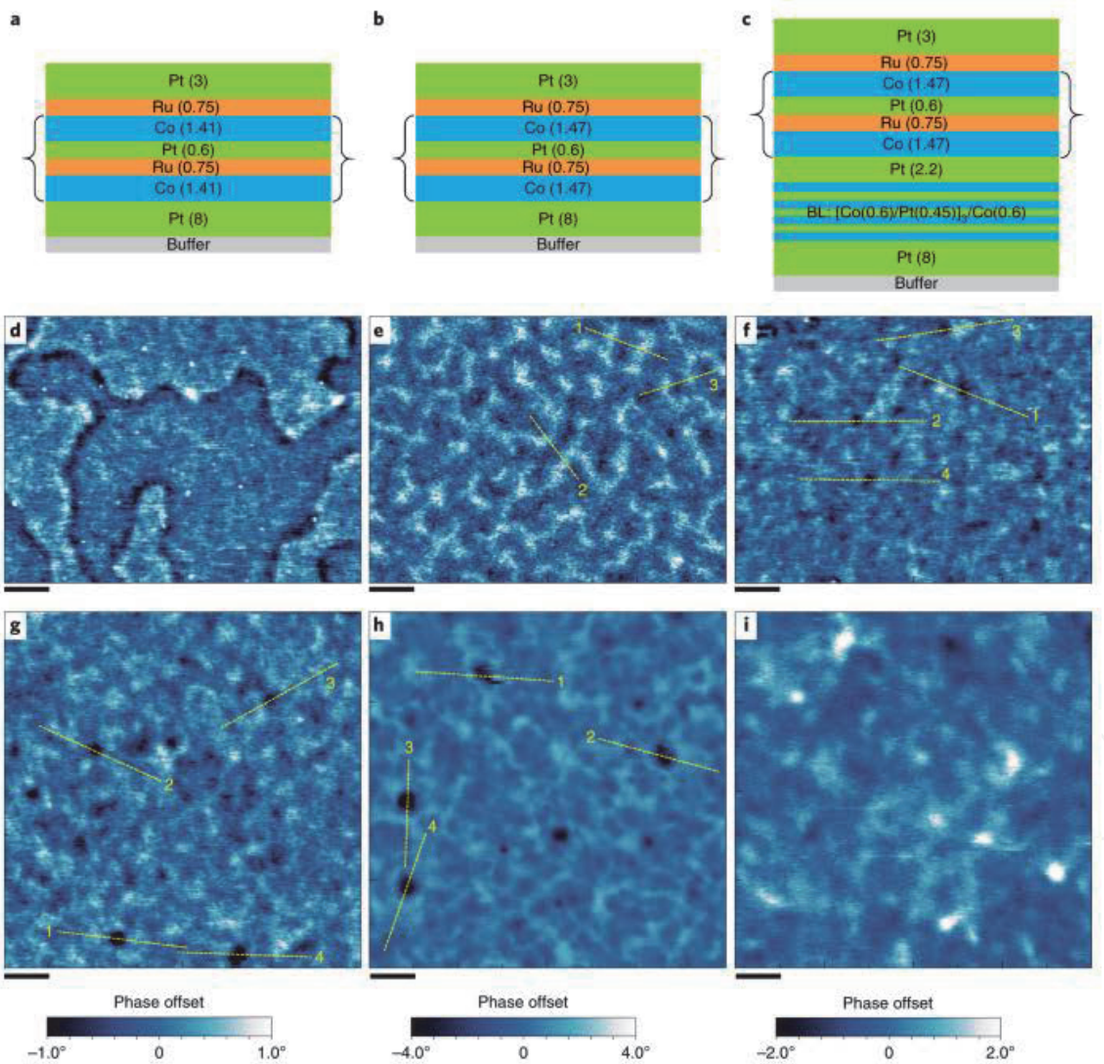

Figure 10.
Multilayer stack for SAF with substantial effective PMA (a), SAF with vanishing effective PMA (b) and BL-SAF system (c). Brackets indicate the SAF system, layer thicknesses are given in nanometers. Note that t_{Co} = 1.41 nm is well below whereas t_{Co} = 1.47 nm is very close to the spin reorientation thickness previously determined. d, MFM image of SAF with effective PMA at 0 mT. e, MFM image of SAF with vanishing effective PMA at 0 mT. f, MFM image of BL-SAF at 0 mT, after saturation of the BL under an external perpendicular field $\mu_0 H_{ext}$ = 60 mT. g–i, MFM observations of the BL-SAF system under external applied perpendicular field for $\mu_0 H_{ext}$ = 20 mT (g), for $\mu_0 H_{ext}$ = 60 mT (h) and for $\mu_0 H_{ext}$ = 100 mT (i). Scale bars, 500 nm. All MFM images in d–g share the same color scale shown below g, while MFM images in panels h, i use different scales, all indicating the phase offset in lift mode. Yellow dashed lines in panels e–h indicate line sections of the MFM image.

2.3 Antiferromagnetic materials

The skyrmions hosted in ferromagnets are that has two difficulties that is stabilization of ultrasmall skyrmion due to the dipolar interaction and to stabilize individual skyrmions without using the external magnetic fields [17, 19, 21]. In antiferromagnets, two coupled equivalent magnetic subsystems align antiparallel to each other with no net magnetic moment, thus dipolar fields is absent. This forbid dipolar interactions has attracted researchers extremely interesting to use in skyrmions. MFM image obtained for the in the $4 \times 3\mu m^2$ image as shown in **Figure 10**. The domains in uniform antiferromagnetic configurations with generated the small separation between the two compensating magnetic layers. Perpendicular magnetic ansisotropy and the 1.41 nm is below the 1.47 nm. The spin spiral perodicity constitute the independent measurement of the DMI amplitude for system.

3. Half skyrmions

α Fe_2O_3 is a clasical antiferromagentic materiasl which shows the weak ferromagentic behavior due to the presence of DMI in the material. It crystallizes in the R-3c space group with Néel temperature of 948 K. It also exhibits a Morin transiton in which the spin in-plane at room temperature changes to perpendicular direction [22]. Recently, it was shows that the fabricating the α Fe_2O_3 thin films on the A_2O_3 substrate showed that three possible antiferromagentic (AFM) domain orientations. From the PEEM measurement has visually confirmeed the formation of the Votex state of the Meron which are the half skyrmions and anti-vertex called the Anti-merons as shown in **Figure 11(a)** [23]. When α Fe_2O_3 was exchanged coupled with the ferromagentic Cobalt film of 1 nm thick. The interfacial exchange interaction were able to imprint the AFM on the cobalt thin film as shown in the **Figure 11(b)**. The imprinting of the AFM domains on the cobalt by interfacial exchange with the adjacent AFM vortex/anti-vortex in the α-Fe_2O_3 film. **Figure 11(c)** shows the magnetization in the inplabne of the film. **Figure 11(d)** shows the smearing of the Co vector map. They have also able to manupuulate the meron pairs by the small magnetic field of 100 mT in plane to the [110] direction. This proved that the cobalt layer aligns with the α-Fe_2O_3 and with the staggeres magnetization the majority of the merons have seen disappeared.

Recently the Antiferromagnetic half-skyrmions and bimerons at room temperature was observed [24]. In their study the α-Fe_2O_3 and Rh doped Fe_2O_3 thin films were prepared by pulsed laser deposition and on the top of the film platinum (Pt) was coated on the top of it. For the thin film of α-Fe_2O_3 it showed the Morin transion at 240 K and for Rh doped Fe_2O_3 thin film it was 298 K [25]. It was AFM textures gradually shrink to become fine bubbles and persist up to room temperature for both the films. They have carried out the details analysis by the Néel vector maps of the IP orientations as shown in **Figure 12(a-c)**. In **Figure 12(a)** most of the resions are in the out of plane oriented and display in-plane winding, due to the mixing of the Bloch- and Néel-type domain-wall. They also indicates that the small in-plane islands nucleating inside the out of plane matrix have random in-plane orientations consistent with the first-order nature of the Morin transition. When the temperature is near to the morin transition the out of plane regions shrink and in-plane islands widen considerably and merging with each other if in close proximity as shown **Figure 12(b)**. When the temperature is above the morin transition the AFM textures in which spins are predominantly lying along the basal planes, separated by 60 domain wall **Figure 12(c)**. When a region of out of plane spins

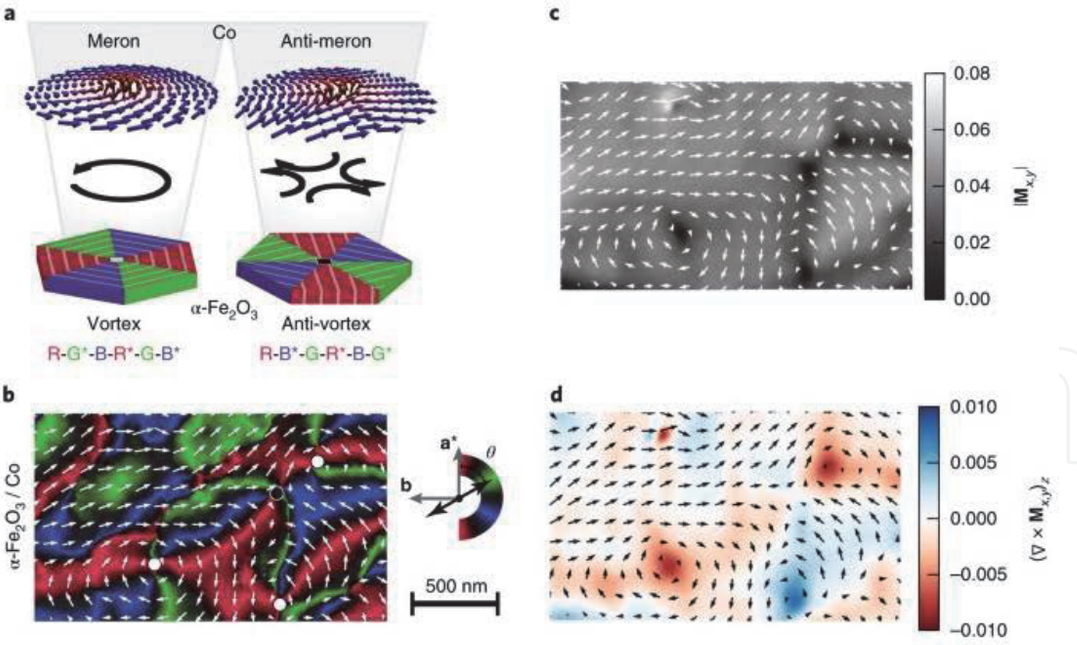

Figure 11.
(a) Shows the Merons (vortices) and anti Merons (anti-vortex) in the α-Fe_2O_3. (b) Domain images of the co and α-Fe_2O_3 thin film, (c) measured magnitude of Co magnetization in the sample plane and (d), z component of the curl of the Co vector map [23].

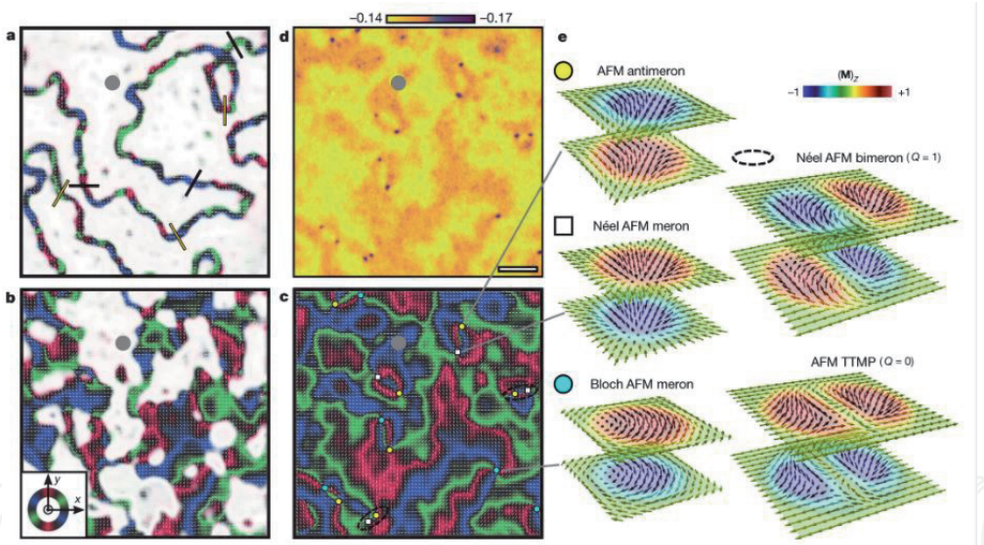

Figure 12.
(a–c) Are the vector-mapped images from the LH-PEEM images afor theα-Fe_2O_3–Pt interface. (a) Temperature less than morin transition, (b) temperature near to morin transition and (c) temperature greater than morin transition. (d) Shows AFM ouf of plane bubbles lying at the core of the corresponding to anti-vertices in 1 μm scale bar [24].

happens to be encircled by in-plane spins, the out of plane bubble becomes trapped and shrinks to a very small size and does not disappear because it is topologically forbidden from unwinding completely into the plane **Figure 12(d)**.

4. Conclusion

From this chapter the various presence of the skyrmions in the multilayer, monolayer and non-centrosymmetric layer have been discussed in detail and the finally the recent advances in the observation of the half skyrmion were also

discussed. For the device application thin film heterostructures are very important. This will lead to the future skyrmion based devices for the manipulation by optical, current, electric field and also by the spin orbit torque devices. So that the infomation can be used for the racetrack based memory devices and logic implementation.

Acknowledgements

The author wants to acknowledge IIT Kharapur for SRF funding.

Conflict of interest

The authors declare no conflict of interest.

Author details

Rajesh Kumar Rajagopal
School of Nanoscience and Technology, Indian Institute of Technology Kharagpur, Kharagpur, West Bengal, India

*Address all correspondence to: r.g.rajeshkumarr@gmail.com

References

[1] Bogdanov A and Hubert A 1994 J. Magn. Magn. Mat. 138 255 DOI: 10.1016/0304-8853(94)90046-9

[2] Kanazawa N, Seki S and Tokura Y 2017 Adv. Mater. 29 1603227 DOI: 10.1002/adma.201603227

[3] Bogdanov A and Yablonskii D 1989 Sov. Phys. JETP 68 101

[4] Mühlbauer S, Binz B, Jonietz F, Pfleiderer C, Rosch A, Neubauer A, Georgii R and Böni P 2009 Science 323 915 DOI: 10.1126/science.1166767

[5] Yu X Z, Onose Y, Kanazawa N, Park J H, Han J H, Matsui Y, Nagaosa N and Tokura Y 2010 Nature 465 901 DOI: 10.1038/nature09124

[6] Seki S, Yu X Z, Ishiwata S and Tokura Y 2012 Science 336 198 DOI: 10.1126/science.1214143

[7] Kosuke Karube, Jonathan S. White, Daisuke Morikawa, Charles D. Dewhurst, Robert Cubitt, Akiko Kikkawa, Xiuzhen Yu, Yusuke Tokunaga, Taka-hisa Arima, Henrik M. Ronnow, Yoshinori Tokura and Yasujiro Taguch, Science Advances 2018: 4, 9, 7043. DOI: 10.1126/sciadv.aar7043

[8] Kézsmárki, S. Bordács, P. Milde, E. Neuber, L. M. Eng, J. S. White, H. M. Rønnow, C. D. Dewhurst, M. Mochizuki, K. Yanai, H. Nakamura, D. Ehlers, V. Tsurkan and A. Loidl 2015 Nat. Mater. 14 1116 DOI: 10.1038/nmat4402

[9] Ajaya K. Nayak, Vivek Kumar, Tianping Ma, Peter Werner, Eckhard Pippel, Roshnee Sahoo, Franoise Damay, Ulrich K. Rößler, Claudia Felser and Stuart S. P. Parkin 2017 Nature 548 561 DOI: 10.1038/nature23466

[10] Stefan Heinze, Kirsten von Bergmann, Matthias Menzel, Jens Brede, André Kubetzka, Roland Wiesendanger, Gustav Bihlmayer and Stefan Blügel Nature Physics volume 7, 713–718, 2011 DOI: 10.1038/nphys2045

[11] Niklas Romming, Christian Hanneken, Matthias Menzel, Jessica E. Bickel*, Boris Wolter, Kirsten von Bergmann+, André Kubetzka+, Roland Wiesendanger. Writing and deleting single magnetic skyrmions. Science 341, 636–639 (2013) DOI: 10.1126/science.1240573

[12] S. A. Meynell, M. N. Wilson, K. L. Krycka, B. J. Kirby, H. Fritzsche, and T. L. Monchesky Phys. Rev. B 96, 054402, 2017 DOI:10.1103/PhysRevB.96.054402

[13] Charles S. Spencer, Jacob Gayles, Nicholas A. Porter, Satoshi Sugimoto, Zabeada Aslam, Christian J. Kinane, Timothy R. Charlton, Frank Freimuth, Stanislav Chadov, Sean Langridge, Jairo Sinova, Claudia Felser, Stefan Blügel, Yuriy Mokrousov, and Christopher H. Marrows 2018 Phys. Rev. B 97 214406 DOI: 10.1103/PhysRevB.97.214406.

[14] Meynell S A, Wilson M N, Fritzsche H, Bogdanov A N and Monchesky T L 2014 Phys. Rev. B 90 014406 DOI: 10.1103/PhysRevB.90.014406

[15] Dupé, B., Hoffmann, M., Paillard, C. and Heinze, S. Nat. Commun. 5, 4030 (2014) DOI: 10.1038/ncomms5030

[16] Hongxin Yang, André Thiaville, Stanislas Rohart, Albert Fert, and Mairbek Chshiev. Phys. Rev. Lett. 115, 267210 (2015) DOI: 10.1103/PhysRevLett.115.267210

[17] C. Moreau-Luchaire, C. Moutafis, N. Reyren, J. Sampaio, C. A. F. Vaz, N. Van Horne, K. Bouzehouane, K. Garcia, C. Deranlot, P. Warnicke, P. Wohlhüter, J.-M. George, M. Weigand, J. Raabe, V. Cros and A. Fert. Nature

Nanotechnology 11,444–448 (2016) DOI: 10.1038/nnano.2015.313

[18] Swekis P, Markou A, Kriegner D, Gayles J, Schlitz R, Schnelle W, Goennenwein S T B and Felser C 2019 Phys. Rev. Mater. 3 013001 DOI: 10.1103/PhysRevMaterials.3.013001

[19] Olivier Boulle, Jan Vogel, Hongxin Yang, Stefania Pizzini, Dayane de Souza Chaves, Andrea Locatelli, Tevfik Onur Menteş, Alessandro Sala, Liliana D. Buda-Prejbeanu, Olivier Klein1, Mohamed Belmeguenai, Yves Roussigné, Andrey Stashkevich, Salim Mourad Chérif, Lucia Aballe, Michael Foerster, Mairbek Chshiev, Stéphane Auffret, Ioan Mihai Miron and Gilles Gaudin Nature Nanotechnology. 11, 449–454 (2016) DOI: 10.1038/NNANO.2015.315.

[20] Fert A 1990 Mater. Sci. Forum 59-60 439 DOI:10.4028/www.scientific.net/MSF.59-60.439

[21] Seonghoon Woo, Kai Litzius, Benjamin Krüger, Mi-Young Im, Lucas Caretta, Kornel Richter, Maxwell Mann, Andrea Krone, Robert M. Reeve, Markus Weigand, Parnika Agrawal, Ivan Lemesh, Mohamad-Assaad Mawass, Peter Fischer, Mathias Kläui and Geoffrey S. D. Beach Nature Materials 19, 34–42 (2020) DOI: 10.1038/s41563-019-0468-3

[22] Morin, F. J Electrical Properties of α Fe_2O_3 and α Fe_2O_3 Containing Titanium, Phys. Rev., 83, 5, 1005-1010, 1951, DOI: 10.1103/PhysRev.83.1005. url = https://link.aps.org/doi/10.1103/PhysRev.83.1005

[23] F. P. Chmiel, N. Waterfield Price, R. D. Johnson, A. D. Lamirand, J. Schad, G. van der Laan, D. T. Harris, J. Irwin, M. S. Rzchowski, C.-B. Eom and P. G. Radaelli. Observation of magnetic vortex pairs at room temperature in a planar α-Fe2O3/Co heterostructure. Nature Mater 17, 581–585 (2018). DOI: 10.1038/s41563-018-0101-x

[24] Hariom Jani, Jheng-Cyuan Lin, Jiahao Chen, Jack Harrison, Francesco Maccherozzi, Jonathon Schad, Saurav Prakash, Chang-Beom Eom, A. Ariando, T. Venkatesan and Paolo G. Radaelli. Antiferromagnetic half-skyrmions and bimerons at room temperature. Nature 590, 74–79 (2021). DOI: 10.1038/s41586-021-03219-6

[25] Coey, J. M. D. and Sawatzky, G. A. A study of hyperfine interactions in the system $(FeRh_x)_2O_3$ using the Mössbauer effect (bonding parameters). J. Phys. C Solid State Phys. 4, 2386 (1971). DOI: 10.1088/0022-3719/4/15/025.